THE SPITZER SURVEY OF STELLAR STRUCTURE IN GALAXIES (S4G)

Kartik Sheth[1,2,3], Michael Regan[4], Joannah L. Hinz[5], Armando Gil de Paz[6], Karín Menéndez-Delmestre[7], Juan-Carlos Muñoz-Mateos[1,6], Mark Seibert[7], Taehyun Kim[1,24] Eija Laurikainen[8,9], Heikki Salo[8], Dimitri A. Gadotti[10,11], Jarkko Laine[8,9], Trisha Mizusawa[1,2,3], Lee Armus[2,3], E. Athanassoula[12], Albert Bosma[12], Ronald J. Buta[13], Peter Capak[2,3], Thomas H. Jarrett[2,3], Debra M. Elmegreen[14], Bruce G. Elmegreen[15], Johan H. Knapen[16,24], Jin Koda[17], George Helou[2,3], Luis C. Ho[7], Barry F. Madore[7], Karen L. Masters[18], Bahram Mobasher[19], Patrick Ogle[2,3], Chien Y. Peng[20], Eva Schinnerer[21], Jason A. Surace[2,3], Dennis Zaritsky[5], Sébastien Comerón[16,22], Bonita de Swardt[23] Sharon E. Meidt[21], Mansi Kasliwal[3], Manuel Aravena[1]

ABSTRACT

The *Spitzer* Survey of Stellar Structure in Galaxies (S4G) is an Exploration Science Legacy Program approved for the *Spitzer* post-cryogenic mission. It is a volume-, magnitude-, and size-limited (d<40 Mpc, |b| > 30°, m_{Bcorr} <15.5, D_{25} >1′) survey of 2,331 galaxies using the Infrared Array Camera (IRAC) at 3.6 and 4.5μm. Each galaxy is observed for 240 s and mapped to $\geq$ 1.5×D_{25}. The final mosaicked images have a typical 1σ rms noise level of 0.0072 and 0.0093 MJy sr^{-1} at 3.6 and 4.5μm, respectively. Our azimuthally-averaged surface brightness profile typically traces isophotes at $\mu_{3.6\mu m}(AB)(1\sigma) \sim 27$ mag arcsec^{-2}, equivalent to a stellar mass surface density of ~ 1 $M_\odot$pc^{-2}. S4G thus provides an unprecedented data set for the study of the distribution of mass and stellar structures in the local Universe. This large, unbiased and extremely deep sample of all Hubble types from dwarfs to spirals to ellipticals will allow for detailed structural studies, not only as a function of stellar mass, but also as a function of the local environment. The data from this survey will serve as a vital testbed for cosmological simulations predicting the stellar mass properties of present-day galaxies. This paper introduces the survey, describes the sample selection, the significance of the 3.6 and 4.5μm bands for this study, and the data collection & survey strategy. We describe the S4G data analysis pipeline and present measurements for a first set of galaxies, observed in both the cryogenic and warm mission phase of *Spitzer*. For every galaxy we tabulate the galaxy diameter, position angle, axial ratio, inclination at $\mu_{3.6\mu m}(AB)$= 25.5 and 26.5 mag arcsec^{-2} (equivalent to $\approx \mu_B(AB)$=27.2 and 28.2 mag arcsec^{-2}, respectively). These measurements will form the initial S4G catalog of galaxy properties. We also measure the total magnitude and the azimuthally-averaged radial profiles of ellipticity, position angle, surface brightness and color. Finally, we deconstruct each galaxy using GALFIT into its main constituent stellar components: the bulge/spheroid, disk, bar, and nuclear point source, where necessary. Together these data products will provide a comprehensive and definitive catalog of stellar structures, mass and properties of galaxies in the nearby Universe and enable a variety of scientific investigations, some of which are highlighted in this introductory S4G survey paper.

Subject headings: galaxies: evolution — galaxies: formation — galaxies:structure

[1] National Radio Astronomy Observatory / NAASC, 520 Edgemont Road, Charlottesville, VA 22903
[2] Spitzer Science Center
[3] California Institute of Technology, 1200 East California Boulevard, Pasadena, CA 91125
[4] Space Telescope Science Institute, 3700 San Martin Drive, Baltimore, MD 21218
[5] University of Arizona, 933 N. Cherry Ave, Tucson, AZ 85721
[6] Departamento de Astrofsica, Universidad Complutense de Madrid, Madrid 28040, Spain
[7] The Observatories, Carnegie Institution of Washington, 813 Santa Barbara Street, Pasadena, CA 91101
[8] Department of Physical Sciences/Astronomy Division, University of Oulu, FIN-90014, Finland
[9] Finnish Centre for Astronomy with ESO (FINCA), University of Turku
[10] Max-Planck-Institut für Astrophysik, Karl-Schwarzschild-Strasse 1, D-85748 Garching bei Mnchen, Germany
[11] European Southern Observatory, Casilla 19001, Santiago 19, Chile
[12] Laboratoire d'Astrophysique de Marseille (LAM), UMR6110, Université de Provence/CNRS, Technopôle de Marseille Etoile, 38 rue Frédéric Joliot Curie, 13388 Marseille Cédex 20, France
[13] Department of Physics and Astronomy, University of Alabama, Box 870324, Tuscaloosa, AL 35487, USA
[14] Vassar College, Dept. of Physics and Astronomy, Poughkeepsie, NY 12604
[15] IBM Research Division, T.J. Watson Research Center, Yorktown Hts., NY 10598
[16] Departamento de Astrofísica, Universidad de La Laguna, Spain
[17] Department of Physics and Astronomy, SUNY Stony Brook, Stony Brook, NY 11794-3800
[18] Institute of Cosmology and Gravitation, University of Portsmouth, Dennis Sciama Building, Burnaby Road, Portsmouth, PO1 2EH, UK
[19] Department of Physics and Astronomy, University of California, Riverside, CA 92521
[20] NRC Herzberg Institute of Astrophysics, 5071 West Saanich Road, Victoria, V9E 2E7, Canada
[21] Max-Planck-Institut für Astronomie, Königstuhl 17, 69117 Heidelberg, Germany
[22] Korea Astronomy and Space Science Institute, 838, Daedeokdae-ro, Yuseong-gu, Daejeon, 305-348, Republic of Korea

1. INTRODUCTION

Understanding the distribution of stars within a galaxy is akin to the study of the endoskeleton of a body; embedded within the galaxy is the fossil record of the assembly history and evolutionary processes of cosmic time. The first step in unraveling this history is to obtain a complete census of the stellar structures in galaxies in the local volume. This is the primary motivation for the *Spitzer* Survey of Stellar Structures in Galaxies (S^{4}G). S^{4}G is a volume-limited (d < 40 Mpc), size-limited (D$_{25}$ >1′) and apparent B-band brightness (corrected for inclination, galactic extinction and K-correction) limited (m$_{Bcorr}$ <15.5) survey of 2,331 nearby galaxies at 3.6 and 4.5μm with the Infrared Array Camera (IRAC) (Fazio et al. 2004) on the *Spitzer* Space Telescope (SSC) (Werner et al. 2004).

Over the last 70 years, numerous surveys have sought to create baseline data sets for nearby galaxies with as few as tens of galaxies (ANGST: Dalcanton et al. 2009; SINGS, Kennicutt et al. 2003) to tens of thousands of galaxies (e.g., RC3, de Vaucouleurs et al. 1991). While these surveys was designed specifically for particular scientific goals, none of them provides an accurate inventory of the stellar mass and the stellar structures in nearby galaxies. The main reason is that infrared surveys, where light from the old stellar population is better measured due to reduced dust extinction and contamination from star formation, are extremely difficult to conduct from the ground. The largest ground-based infrared surveys (e.g., 2MASS, Skrutskie et al. 2006; DE-NIS, Epchtein et al. 1994; Paturel et al. 2003) are rather shallow in depth, and as a result, studies of nearby galaxies have been restricted to high surface brightness inner disks. In contrast, deeper infrared surveys (e.g., OS-UBGS, Eskridge et al. 2002, NIRSOS, Laurikainen et al. 2010) have imaged only a few hundred galaxies. S^{4}G is specifically designed to provide over an order of magnitude improvement in the sample size and several magnitudes deeper data than existing surveys.

S^{4}G builds upon the two previous *Spitzer* Legacy surveys of nearby galaxies: SINGS (Kennicutt et al. 2003) and the Local Volume Legacy Survey (LVL) (Lee et al. 2008). SINGS was designed to probe star formation, dust and polycyclic aromatic hydrocarbon (PAH) emission in all representative environments *within* galaxies in a sample of 75 objects. The LVL survey was designed to study spatially-resolved star formation and the red stellar population within galaxies in a local volume of 11 Mpc. The local volume limits the 258 LVL galaxies to consist mostly of dwarf, irregular and late type systems (see green histogram in Fig. 1). The remainder of the *Spitzer* archive from the cryogenic mission is inadequate for the science goals outlined here because it lacks sufficient numbers of galaxies of all stellar masses, particularly at M$_*$ < 10^9 $M_\odot$, Hubble types and environments. As shown in Figures 1 and 2, S^{4}G explores the full range of stellar structures in a representative and large sample of galaxies of all types, masses and in diverse environments. S^{4}G is designed to provide the ultimate baseline data set for the study of stellar structures and mass in nearby galaxies.

In this paper we introduce S^{4}G, describe the data collection and analysis strategy and briefly describe the
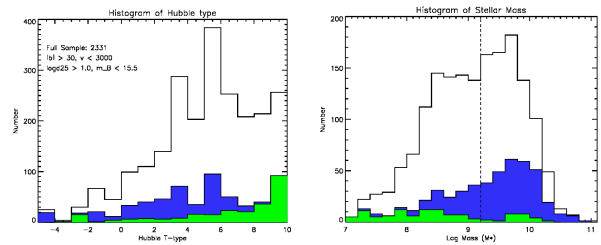

FIG. 1.— *Left:* Histogram of all galaxies in S^{4}G as a function of the Hubble T-type shown in black. The green and blue filled histograms show archival data from the LVL (green) and other GO/GTO data (blue). *Right:* Histogram of masses for the S^{4}G sample galaxies shown in black, where masses are calculated from the 2MASS photometry assuming the M/L function from (Bell et al. 2003). The biggest gains in building a statistically complete sample are for galaxies with log (M/$M_\odot$) < 9.2.
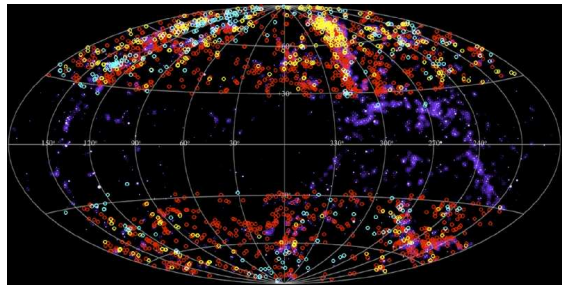

FIG. 2.— Galaxies from S^{4}G plotted on the local large scale structure map from the 2MASS XSC (Jarrett 2004) shown in purple. The red circles show the warm mission S^{4}G galaxies to be observed. The cyan and yellow circles show LVL and GO/GTO archival galaxies. With the full S^{4}G sample, we will have the ability to make a less biased study of the galaxy host properties as a function of the local large scale structures.

variety of scientific investigations possible with these data. All S^{4}G galaxies are processed through a uniform pipeline to create the deepest and largest mid-infrared image catalog of nearby galaxies to date. For every galaxy we measure the magnitude and surface brightness and tabulate the galaxy diameter, position angle, axial ratio, and inclination at $\mu_{3.6\mu m}$ (AB) = 25.5 and 26.5 mag arcsec^{-2}. We also compute the azimuthally-averaged radial profiles of ellipticity, position angle, surface brightness and color. This fundamental catalog of galaxy properties will allow us to classify their morphology based on their stellar structures – a preliminary study is presented in Buta et al. (2010). In the long term, the main goal of the S^{4}G project is to obtain a detailed understanding of the properties of the different stellar structures, their formation and evolutionary paths and their role in the broader picture of galaxy evolution. This will be done by decomposing every galaxy into its constituent structural components (e.g., bulge/spheroid, bar, disk, nuclear point source) using GALFIT (Peng et al. 2002, 2010).

A number of scientific studies are already under way by the S^{4}G team. These include a study of outer disks to determine the variety and frequency of different disk profile(s), truncations or thresholds and their relationship to the build up of galaxy disks, a study of shells and debris around galaxies and their relationship to central star formation or AGN activity, an analysis of the structural properties of bulges/spheroids (classical, disky, boxy/peanut-shaped), determination of the bar

fraction and bar properties in relationship to the host galaxies and environment, an analysis of the stellar arm-interarm variations in spirals, an investigation of the underlying old stellar population in rings and a search for fossil rings, an analysis of the old stellar content of dwarf galaxies and its implication for their formation history, etc. Longer term studies include star formation history and assembly of galaxies using *GALEX* and Hα data, the Tully–Fisher relationship using existing HI data (e.g., ALFALFA, Giovanelli et al. 2005, HIPASS, Barnes et al. 2001), and testing of new mid-infrared diagnostics of AGN. We describe these studies in more detail in §6. Ultimately, S^{4}G will lead to numerous other studies of astrophysical phenomena in the nearby Universe and provide a key anchoring data set for studies of galaxy evolution.

2. THE *SPITZER* 3.6 AND 4.5μM BANDS: BEST TRACERS OF STELLAR MASS

The 3.6 and 4.5μm IRAC bands on *Spitzer* are ideal tracers of the stellar mass distribution in galaxies because they image the Rayleigh–Jeans limit of the blackbody emission for stars with T > 2000 K. Moreover, the mid-infrared [3.6]–[4.5] color in nearby galaxies is nearly constant with radius, and independent of the age of the stellar population and its mass function (Pahre et al. 2004). Analysis of the tilt in the fundamental plane for ellipticals shows that the *Spitzer* IRAC bands are better tracers of the stellar mass than even K-band emission, which is more sensitive to variations in the underlying stellar population; the IRAC data are more uniform and therefore are the best and perhaps most direct tracers of stellar mass (Jun & Im 2008). Additionally, on *Spitzer* these bands are so sensitive that S^{4}G will image to extremely low stellar mass surface densities ($\sim 1 M_\odot$pc^{-2}).

There are minor contaminants to the old stellar population light in the 3.6 and 4.5μm IRAC bands. In the 3.6μm band, there is a very weak 3.3μm PAH feature, which contributes negligibly to the overall emission in the band (< 2% as the equivalent width is $\sim$0.02μm, Tokunaga et al. 1991). Hot dust (T$_d$ >500K) from very small grains can contribute light to both bands with a higher contribution in the 4.5μm band, but this condition occurs only near active galactic nuclei or extreme starbursts. By examining the colors of the galaxies, we should be able to use the two IRAC bands to remove the effects of the 3.3μm PAH or hot dust emission. Another important advantage of having 2 bands is that by co-adding them, we can further improve the signal to noise and push the study to even fainter regions of the galaxies. In both bands, the contamination from young red supergiants is also very low. From previous studies, it is known that in the near-infrared, the overall contamination from young red supergiants to a galaxy is only $\sim$3% but in regions of star formation, the contribution may be as high as 25% (Rhoads 1998). These regions, however, are easily identifiable and can be flagged. At the IRAC wavelengths, the fractional contribution from star-forming regions is expected to be the same (or lower) because these wavebands are at longer wavelengths on the Rayleigh–Jeans tail of the spectral energy distribution. At these wavelengths, there is lower dust extinction (Draine & Lee 1984) and no other significant emission sources. Thus, with the extremely low surface bright-

ness limits, S^{4}G offers a unique and virtually dust-free view of the distribution of mass in stellar structure in the nearby Universe.

Although ground-based near-infrared observations can offer higher angular resolution than *Spitzer*, the main obstacle for ground-based observations is the very high and variable sky brightness (typically $\mu_K \sim 13.4$ mag arcsec^{-2}). The surface brightness level in the IRAC data is over 10 magnitudes below the typical sky brightness level. To get to this level from the ground, one would need to characterize the sky brightness, the flat field and instrumental variations to better than 0.0009%. This is currently not possible with any existing (or planned) near-infrared survey. Surveys like UKIDSS LAS or VISTA VHS are planning to reach a depth of 18.4 (21.2 in AB) mag arcsec^{-2} in the K$_s$ band, which translates to 30 $L_\odot$pc^{-2} (even with the brighter stellar emission at K$_s$ band), whereas S^{4}G reaches $\sim$ 2 $L_\odot$pc^{-2}. It is the stability of the background that is the biggest advantage for space-based observations.

3. SAMPLE SELECTION

We chose all galaxies with radial velocity V$_{radio}$ < 3000 km/s (corresponding to a distance d < 40 Mpc for a Hubble constant of 75 km/s/Mpc), total corrected blue magnitude m$_{Bcorr}$ < 15.5, blue light isophotal angular diameter D$_{25}$ > 1.0 arcmin at galactic latitude |b| > 30° using HyperLEDA (Paturel et al. 2003). The choice of V$_{radio}$ does limit the sample to galaxies with a radio-derived (e.g., HI) radial velocities in HyperLEDA, and as a result misses some galaxies for which only optically-derived radial velocities exists; currently, a sample chosen with V$_{optical}$ instead of V$_{radio}$ would contain 2997 galaxies. A comparison of the galaxy properties of the two samples shows that the S^{4}G sample misses galaxies that are small, relatively faint and early-type (gas-poor) systems from the volume surveyed.

We also note that our sample was defined using HyperLEDA in September 2007 - since then 98 more galaxies have been added to the HyperLEDA data base that meet the S^{4}G criteria described above and we expect that some more may be added as better data become available. Given the limited lifetime of *Spitzer*, we are unable to go back and acquire data on these additional galaxies but we expect that the few percent additional galaxies will not strongly influence the core characteristics of the sample, except for the bias against early-type galaxies as noted above.

The choice of a 40 Mpc volume is arbitrary – it was chosen to be large enough to provide a statistically significant number of galaxies of all types and to be representative of a large range of the local large scale structure environment (as shown in Fig. 2). Our experience with previous surveys of galaxy properties (e.g., Sheth et al. 2008) has shown that a few thousand galaxies are needed to accurately measure and account for completeness effects in mass, color and size selection of galaxy samples for robust investigations of relationships between galactic structure and host galaxy properties. The size cut, log D$_{25}$ > 1.0, was made to ensure that galaxies were large enough for a detailed study of their internal structure (at 40 Mpc, 1′ $\sim$11.6 kpc). The apparent size and apparent magnitude cut were chosen to match the RC3

limits. The galactic latitude cut, $|b| > 30°$, was used to minimize the unresolved Galactic light contribution from the Milky Way disk. The full sample of 2,331 S^{4}G galaxies is listed in Table 1. In Figure 1, we show the distribution of S^{4}G galaxies as a function of Hubble type and stellar mass, along with the existing distribution of the LVL galaxies (green) and GO/GTO galaxies (blue) including the SINGS galaxies. There are some noteworthy sub-samples within S^{4}G . There are 188 early-type galaxies (ellipticals and lenticulars), 206 dwarf galaxies (defined as $M_B > -17$), of which 135 are DDO dwarfs and 465 edge-on ($i > 75°$) systems. Also over 800 of the S^{4}G galaxies are mapped beyond a diameter of $3 \times D_{25}$. These sub-samples provide the deepest, largest and most homogeneous samples for a multitude of galaxy evolutionary studies, some of which are described in §6.

3.1. *Archival / Cryogenic* Spitzer *Data*

Of the 2,331 galaxies in the S^{4}G sample, 597 had some existing data at 3.6 and 4.5μm from the *Spitzer* cryogenic mission. 125 of these are part of the LVL survey and 56 are from the SINGS survey, both of which used the same observing strategy (§4) we employ for S^{4}G . Almost all of the archival maps have at least 240 s of integration time per pixel and are sufficiently deep. The only exceptions are NGC 5457 (96s), NGC 0470, NGC 0474 (150s), and NGC 5218, NGC 5216, and NGC 5576 (192s).

In terms of area, 82 of the archival galaxies were mapped between 1.0 and $1.5 \times D_{25}$, and 43 others were mapped to $< 1.0 \times D_{25}$. While outer disk science for these 125 galaxies would benefit from an extended map, they represent only a small fraction of the total sample, and the repetition of observations would have yielded only an incremental scientific return. Therefore, we decided not to repeat observations of any of the archival galaxies. We also decided not to map the SMC and the LMC, which meet our selection criteria but are very large and are being observed as part of other GO programs. M33, the other commonly studied Local Group galaxy was observed during the cryogenic mission and is included in the archival part of our sample. All other galaxies that were found via the HyperLEDA data base search in 2007 September are observed (see note earlier about the modest additions to the HyperLEDA database in the last three years). Although we do not repeat observations of any of the archival galaxies, we are processing all galaxies in the S^{4}G sample, except the SMC and LMC, through the same S^{4}G reduction and analysis pipelines described in §5.

4. *SPITZER* POST-CRYOGENIC MISSION OBSERVATIONS STRATEGY

The 1,734 S^{4}G galaxies being observed in the post-cryogenic mission are mapped using either a small dithered map or a mosaicked observation with both IRAC channels. All galaxies are observed with a total on-source integration time of 240 s which leads to an rms noise of $\mu(1\sigma) \sim 0.0072$ and 0.0093 MJy sr^{-1} at 3.6 and 4.5μm, respectively. This translates to a typical surface brightness sensitivity of $\mu_{AB} \sim 27$ mag arcsec^{-2} or a stellar surface density of 1.13 $M_\odot$pc^{-2} (assuming a solar M_K = 3.33, Worthey 1994; M/L$_K$=1, Heraudeau & Simien 1997) .
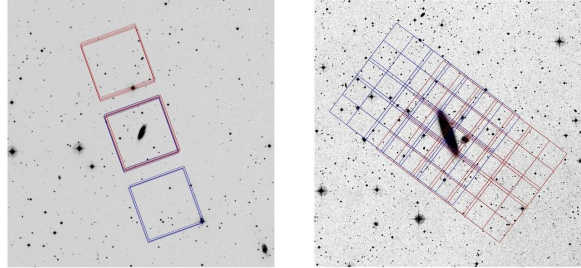

FIG. 3.— *Left:* A typical dithering AOR shown for NGC 2919 in the warm mission. The blue (red) overlay shows the 3.6μm (4.5 μm) coverage. The galaxy is mapped in two separate AORs separated by at least 30 days. The flanking fields are reduced by the S^{4}G pipeline and may also contain serendipitous objects such as interacting galaxies or tidal debris. *Right:* A typical mosaicking AOR shown for NGC 1515 in the warm mission. The blue grid shows the coverage of the 3.6μm camera and the red grid shows the coverage of the 4.5 μm camera. The galaxy is mapped to $>1.5 \times D_{25}$ by both arrays. The mosaicking pattern takes steps of 146.6″ with 30s integrations in each location. The total 240 s integration time is obtained in two separate AORs. Note that significant amounts of sky are also mapped on opposite ends of the galaxy by each of the individual arrays.

1560 of the new observations are of galaxies with $D_{25} < 3.3'$. We can map these galaxies to $1.5 \times D_{25}$ with a single pointing because the *Spitzer* field of view is 5′. Hence all of these galaxies are mapped using a standard cycling small dither pattern with 4 exposures of 30s each in two separate Astronomical Observation Requests (AORs). Each pair of AORs is separated by at least 30 days to allow for sufficient rotation of the telescope so that the galaxy is imaged at two distinct orientations. Two AORs allow us to better remove cosmic rays, and the redundant information gathered by the two visits allows us to characterize and remove image artifacts (e.g., muxbleed, column pulldown, etc (see the IRAC Instrument Handbook[23]) and possible asteroids. Drizzling the data from the two visits also allows us to achieve sub-pixel sampling with which we can reconstruct images with better fidelity than would be possible from a single visit. We also note that since both the 3.6 and 4.5μm arrays collect data simultaneously, their offset placement in the *Spitzer* focal plane means that an additional flanking map is made adjacent to the galaxy in each of the two channels (in some cases, the flanking field from each of the AORs may not overlap exactly due to the telescope rotation, but this does not affect the observations of the main galaxy). An example of a typical dithering AOR is shown in the left panel in Figure 3.

One of the considerations in designing these AORs was the effect of saturation from bright stars on the chip and the scattered light from bright stars falling in one of the three scattering zones surrounding the arrays[24]. Stars brighter than 5th magnitude can leave a latent charge on the chip. Stars brighter than 11th magnitude in the scattering zones may scatter light into the main field of view of the IRAC chips. To mitigate these cases, we used

[23] See http://ssc.spitzer.caltech.edu/irac/iracinstrumenthandbook/
[24] A description of this problem is given in the IRAC instrument handbook at: .http://ssc.spitzer.caltech.edu/irac/iracinstrumenthandbook/

the *Spitzer* Observing Tool (SPOT[25]) to examine every galaxy with a star, $m_{Ks} < 8$ (stars fainter than $m_{Ks} = 8$ do not contribute significantly to the background) within an area of $300''$, covering the IRAC field of view and scattering zones adequately, for all possible visibility windows through 2011. In a majority of these cases, no modifications of AORs were needed because the offending star(s) fell out of the chip or the scattering zones. In the remaining cases, we constructed AORs with timing constraints, slightly offset pointings or used medium dithers or mosaics to reduce the effect of the bright stars.

For galaxies with $D_{25} > 3.3'$, we mosaic them in array coordinates with offsets of $146.6''$ with 30s integrations at each location to create a map $\geq 1.5 \times D_{25}$. This leads to a map with each pixel observed four times at all wavelengths in the core of the map. In addition, on each side of the galaxy there will be a region where each pixel is observed twice but only in one of the two channels. Like the dithered AORs, each mosaic is observed twice but with only a follow-on constraint so that each mosaic overlaps the other closely. An example of this type of an AOR is shown in the right panel of Figure 3.

Although larger mosaics could be made, our experience with SINGS data showed that the dominant noise term comes from variations of the background (Regan & Teuben 2004; Regan et al. 2006). The best background for a galaxy includes sufficient sky not far from the area of interest. Our map sizes are thus fine-tuned to achieve the best possible signal-to-noise for all galaxies.

5. THE S^{4}G PIPELINE

The S^{4}G pipeline is divided into four distinct parts, which we refer to as Pipelines 1, 2, 3 and 4. Pipeline 1 takes the raw basic calibrated data (BCD) fits files and converts them to science-ready data. Pipeline 2 creates a mask for the foreground and background objects for each of the individual galaxies. Pipeline 3 measures the standard global galaxy properties such as size, axial ratio, magnitude, color, etc. and computes the radial profiles of the standard properties. Pipeline 4 deconstructs each galaxy into its major structural components. Each of these is described in detail here.

5.1. *S^{4}G Pipeline 1*

The purpose of pipeline 1 (P1) is to create science-ready mosaics from the two visits of each target. To do this P1 performs two major steps. First, it matches the background level in the individual images to account for drifts in the zero point of the amplifiers. Second, it creates the final mosaic using the Drizzle package of IRAF[26].

To match the background levels in the individual images we find the regions of overlap between all pairs of overlapping images. Typically we require that the overlap region contain 20000 pixels. For all of the new post-cryogenic mission observations (and archival observations that used the same observing strategies), such

an overlap is always available. However, when reducing other archival data with less overlap between the frames, we reduce the number of pixels in the overlap region to as low as 5000 pixels – this still provides an adequate number of pixels for estimating the background.

Within these regions we determine the brightness level of the 20th percentile pixel. We use the 20th percentile brightness level to better avoid detector artifacts such as muxbleed which can affect even the median. By using the 20th percentile brightness level we have a better chance of using the true sky level. We then perform a least square solution using the brightness differences between all the pairs of overlapping images, minimizing the residual background difference. Since we use the difference, we need to use the background level in the first image to set the zero point of the solution. We then make corrected images by adding the solved-for corrections and use these images in the formation of the final mosaic. We create the final mosaic following the standard prescription of the STSDAS DITHER package. This method removes the cosmic rays by first forming a mosaic from a median combination of the images and then comparing the individual images to the median mosaic and flagging any cosmic rays. The final mosaic is formed by drizzling the individual images. The resulting mosaic has a pixel scale of $0.75''$ and we correct for the change in pixel size to keep the units of MJy sr^{-1}.

The relative astrometry of the mosaicked images is excellent because the *Spitzer* pipeline already incorporates the 2MASS positions to update its astrometry for each of the basic calibrated data frames. The S^{4}G pipeline therefore does not require the type of cross-correlation that was needed previously for the SINGS pipeline to align overlapping fields. The relative astrometric accuracy is $<0.''1$.

The point spread function for IRAC is asymmetric and depends on the spacecraft orientation angle. Pipeline 1 images are produced by combining two different visits to the galaxy and therefore we estimate the PSF by combining stars in the foreground and background for six typical S^{4}G galaxies to create a "super"-PSF which has a typical FWHM of $1.''7$ and $1.''6$ at $3.6\mu m$ and $4.5\mu m$ respectively. For the most distant galaxies in our survey at a distance of ~ 40Mpc, this resolution corresponds to a linear scale of ~ 300pc. At the median distance of the galaxies in this survey at 21.6 Mpc, this corresponds to a linear scale of ~ 170pc.

5.2. *S^{4}G Pipeline 2*

After the science-ready images are produced by the S^{4}G pipeline, we generate masks for point sources using SExtractor (Bertin & Arnouts 1996) for both channels. Each mask is checked by eye and iterated to identify any point source otherwise missed by SExtractor. We also unmask any region of the galaxy that may be have been incorrectly identified by SExtractor. The images with their corresponding masks are then run through the third part of the S^{4}G pipeline (Pipeline 3, P3 hereafter).

5.3. *S^{4}G Pipeline 3*

The first step in P3 is to determine the local sky level around each galaxy. We want to be sufficiently far from the galaxy to ensure that there is no contamination from

the galaxy but not so far that the background is not truly local. We do this by computing the median sky value in two concentric elliptical annuli centered at the position of the galaxy. Typically we start the inner annulus at a distance of $1.5 \times D_{25}$. This annulus is divided in azimuth into 45 regions (or sky boxes). Each of these regions is then grown outwards until it encompasses a total of 4000 non-masked pixels[27], as shown in Figure 4. The second annulus begins at the end of the first annulus and the same process is repeated. We compare the measured sky values in the two annuli for any radial gradients which might be indicative of light contamination from the galaxy. If we find that there is contamination, then we move the inner radius outwards and repeat the process until we are assured that we are sampling the local sky.

In our analysis so far, the inner radius of the inner annulus has varied between 1.2 and $2 \times D_{25}$. In all cases for the warm mission data and a majority of the archival data, it has been suffcent to set the inner radius of the annulus to either $1.5 \times$ or $2 \times$ D_{25}. However in a few cases where the archival data are shallow and the galaxy is relatively blue, we moved the inner radius to $1.2 \times D_{25}$ to be immediately outside the galaxy to get as accurate a measurement possible for the local sky level. Automating this procedure is non-trivial because variations at these faint levels ($\mu_{3.6\mu m} > 27$ (AB) mag arcsec^{-2}) can be from a lopsided galaxy, debris or tidal structures, or variation in the background. Therefore we examine every galaxy by eye to ensure that contamination from the galaxy light to the measurement of the sky background is as low as possible and move the radii outwards as needed.

The sky background computation method for three of the galaxies in the S^{4}G sample (NGC 0337, NGC 4450, NGC 4579) is shown in Figure 4. In the central column of this figure, we show an example case for NGC 4450 where the median sky in some of the boxes is affected by the bleeding of flux from a (masked) but saturated nearby bright field star. In such cases we ignore the affected pixels or move the annuli further out to get the best estimate for the background. Finally, we use the standard deviation obtained from the 90 sky boxes with the average standard deviation within each box to estimate the contribution of the low-frequency flat-fielding errors and possible additions to the total error budget in the background determination.

The typical sky brightness level is fainter than 26 (AB) mag arcsec^{-2} at 3.6 and $4.5\,\mu m$. The Poisson noise from the galaxy dominates the total error budget in the central regions, while errors in the sky background are the main source of uncertainty in the outer parts. Large-scale background errors can be particularly significant in galaxies with large apparent sizes. However, in the fainter outer parts, the noise is significantly reduced from azimuthally averaging over a large number of pixels in the outer galaxy – we are therefore able to measure the galaxy profiles well below the typical sky brightness. The typical S/N for a S^{4}G galaxy at the canonical $\mu_{3.6\mu} = 26.5$ (AB) mag arcsec^{-2} is > 3.

The images resulting from Pipeline 1 are calibrated in units of MJy sr^{-1}. The conversion from MJy sr^{-1} to AB

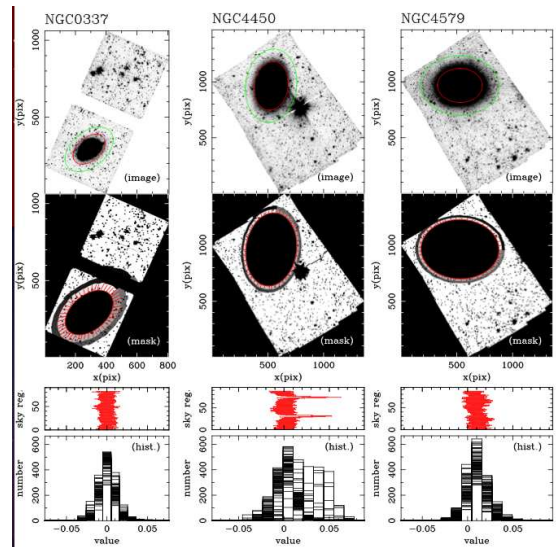[27] For archival galaxies that fill the mosaicked frame, this requirement is reduced to 1000 non-masked pixels.

FIG. 4.— Results of the determination of the sky background for the S^{4}G galaxy NGC 0337, NGC 4450 and NGC4579. Top row: Results for the IRAC 3.6μm image for each galaxy. The D$_{25}$ ellipse is shown in red and inner edge of the annulus from where we begin to estimate the sky is shown in green. Second row: The elliptical annuli used to compute the sky background are shown. The red segments indicate the 45 regions of the inner annulus. The outer annulus used to trace the gradient is shown shaded by the grey scale annulus. The changing shade from light grey to black corresponds to the 45 regions of the outer annulus. In this row all the masked pixels are shown in black but note that the black color of the outer annulus does not mean that these regions are masked. Third row: The median and standard deviation for each of the 90 sky boxes is shown here. Bottom row: A histograms of the pixel values within each of the 90 sky boxes is shown in this panel.

magnitudes is such that the zero-point to convert fluxes in Jy to magnitudes does not vary with wavelength (Oke 1974):

$$m_{AB}(\text{mag}) = -2.5 \log F_\nu(\text{Jy}) + 8.9 \qquad (1)$$

From this definition one can derive the corresponding expression for surface brightness:

$$\mu_{AB}(\text{mag}) = -2.5 \log I_\nu(\text{MJy str}^{-1}) + 20.472 \qquad (2)$$

5.3.1. *P3: Measuring the Galaxy Host Properties*

After the sky level has been properly measured, we use the IRAF routine `ellipse` to determine the radial profiles of intensity, surface brightness, ellipticity and position angle for all galaxies in both bands. The center is determined using `imcenter` and kept fixed during the fit, whereas the ellipticity and position angle are left as free parameters. We generate profiles with two different radial resolutions, by incrementing the semi-major axis in $2''$ and $6''$ at each step, respectively. The latter profiles have a coarser resolution and a better S/N ratio - these are used to measure the RC3-like parameters. The low- and high-frequency sky background errors described above, together with the Poisson noise of the source along each isophote, are considered together in the final error budget of the surface photometry at each radius (see Gil de Paz et al. 2005; Muñoz-Mateos et al. 2009). The errors in the position angle and ellipticity at each radius are computed by the ellipse task from the rms of the pixel values along each fitted isophote. The
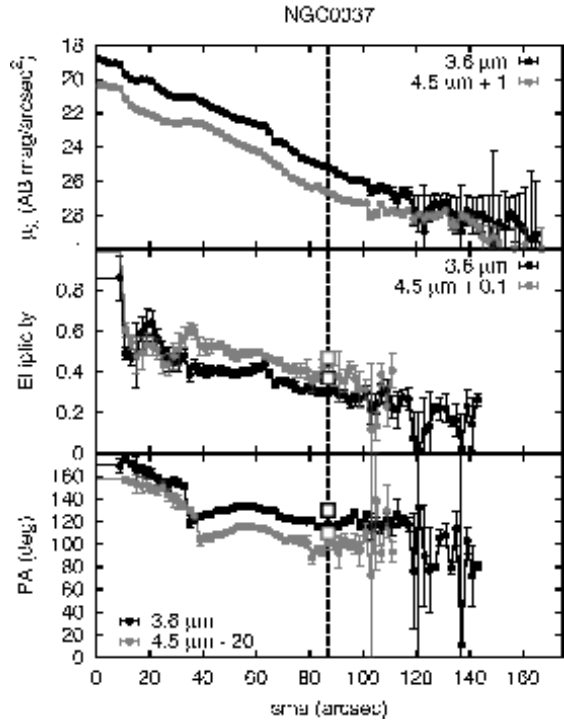
Fig. 5.— Surface photometry results for the S^{4}G galaxy NGC 0337. Top: Surface brightness profiles for 3.6μm (black filled circles) and 4.5μm+1 mag (grey filled circles). The vertical dashed line shows the position of the B-band D$_{25}$ major axis radius. Middle: Variation of the ellipticity of the best-fitting isophote with the radius. For the sake of clarity we have applied an offset of 0.1 to the 4.5μm profile. Bottom: Position Angle of the best-fitting isophote as a function of radius. Note the 20 dg offset applied to the 4.5μm profile. The boxes drawn at the position of the D$_{25}$ major axis radius in the latter two panels indicate the ellipticity and PA listed in the RC3 catalog, respectively.

Fig. 6.— The same as Figure 5, for NGC 4450.

Fig. 7.— The same as Figure 5, for NGC 4579.

corresponding errors for the values of these geometrical parameters at 25.5 and 26.5 (AB) mag arcsec^{-2} are interpolated between the corresponding adjacent values. The error in the semi-major axis is computed from the change in the radius affected by moving the surface brightness profile by the measured errors and an additional 10% error added in quadrature to the measured errors. The 10% error is an estimate of the aperture correction uncertainty as estimated by the Spitzer Science Center instrument team. We compute the error in the semi-major axis for each galaxy. Sample results for NGC 0337 and NGC 4579 are noted below. For NGC 4450, the scattered light from a background star strongly affects the computation of the surface brightness error and therefore the error in the semi-major axis that is unrealistic. In such cases, the error in the semi-major axis can be assumed to be the median semi-major axis error in the S^{4}G sample. The maximum error in the determination of the semi-major axis is 6$''$, the step size of the coarse resolution fitting procedure. In Figures 5, 6 and 7 we show three sample sets of profiles for three galaxies in the sample: NGC 0337 (SBd), NGC 4450 (SAab) and NGC 4579 (SABb). The basic RC3-like galaxy properties (semi-major axis, axial ratio and position angle) are tabulated at the levels of 25.5 and 26.5 (AB) mag arcsec^{-2} in both the 3.6μm and the 4.5μm images, and are quoted in Table 2.
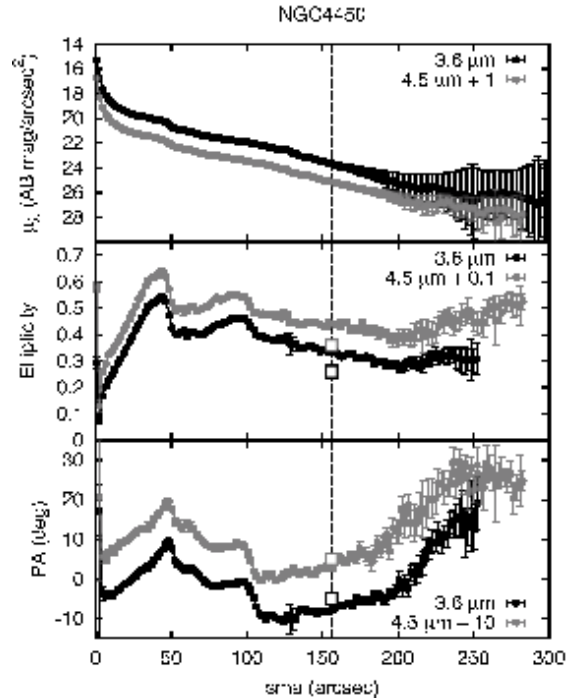
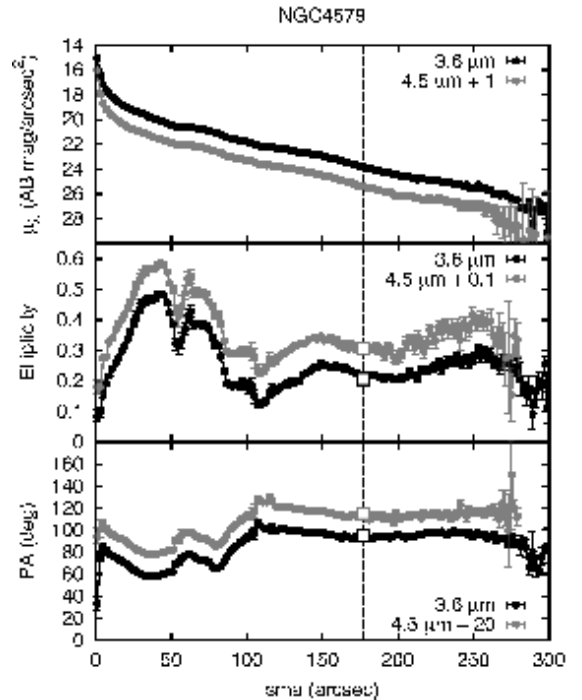Along with the surface photometry we also measure the curve of growth (e.g., Muñoz-Mateos et al. 2009; Gil de Paz et al. 2007) with the integrated flux up to each radius. By fitting the accumulated magnitude as a function of the magnitude gradient at each point we obtain the asymptotic magnitude as the y-intercept of that fit (see Gil de Paz et al. 2007). Once the total magnitude is known, it is straightforward to locate the radii containing a given percentage of the total galaxy lumi-
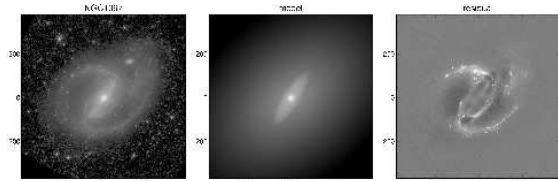
FIG. 8.— Five-component decomposition model for NGC 1097.
The panels show the observed 3.6 micron image (left), the
model image (middle), and the normalized residual image (OBS-
MODEL)/MODEL (right). North is up and east is to the left per
the usual conventions and the units are in arcseconds. The decom-
position includes bulge, disk, bar, central point source and nuclear
ring components, as illustrated in Fig 9. Note how the residual
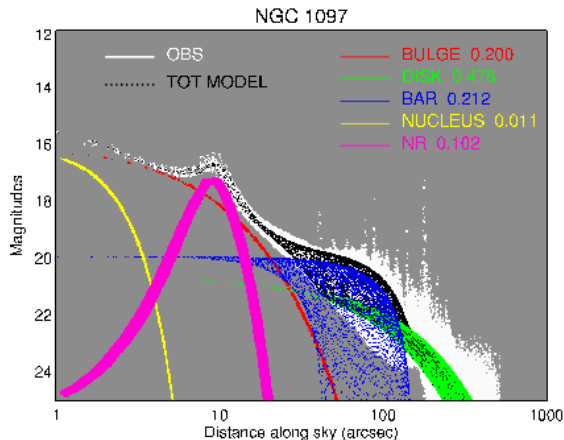image emphasizes the outer spiral and the inner ring structures.

FIG. 9.— The different sub-components of the NGC1097 fit in
Fig. 8. The white dots show the magnitude of each pixel of the
observed image, as a function of distance from the galaxy cen-
ter along the sky plane, while the dark points indicate the total
model. The different colors indicate different sub-components: the
numbers after the labels indicate the relative contribution of the
component to the total model flux. In this type of plot axially
symmetric components appear as curves, while non-axisymmetric
components (i.e. the bar) fill a region confined by their major and
minor axis profiles. Similar plots have been used to visualize BD-
BAR (Laurikainen et al. 2005, 2009) and BUDDA (Gadotti 2008)
decompositions.

nosity, from which concentration indices can be deter-
mined. In Table 3 we quote the asymptotic magnitudes
of the three sample galaxies considered here, together
with the C_{31} (de Vaucouleurs et al. 1977) and C_{42} (Kent
1985) concentration indices.

5.4. S^4G Pipeline 4

In Pipeline 4, we decompose the two-dimensional
stellar distribution in each galaxy into different sub-
components using the version 3 of GALFIT (Peng et al.
2002, 2010). GALFIT is a parametric fitting algorithm
that offers a large flexibility on the fitted models; the op-
timal solution for the model parameters is found with the
Levenberg-Marquardt algorithm, performing non-linear
least-squares χ^2 minimization of the difference between
observed and model images. For our pipeline, we could
have also used BUDDA (Gadotti 2008) and BDBAR
(Laurikainen et al. 2005). We tested all three algorithms
using a set of galaxy images and verified that GALFIT
produces the same results as BUDDA and BDBAR if the
three codes are run with the same set of input images,
models and initial parameters. We chose GALFIT be-
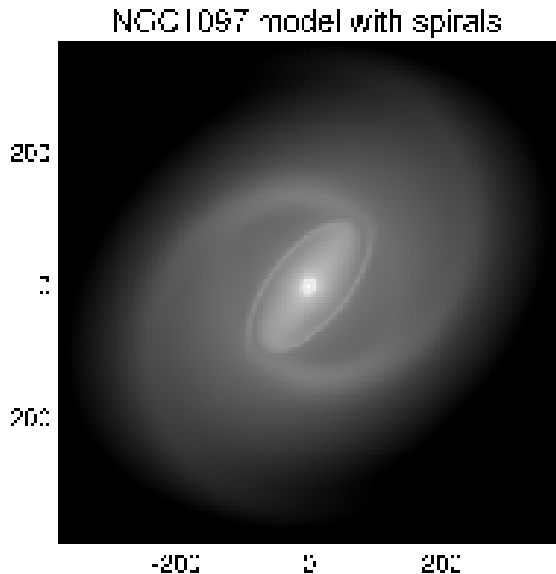cause it is currently the most sophisticated algorithm,

FIG. 10.— Illustration of the capabilities of GALFIT3.0: a de-
composition for NGC 1097 including spiral sub-components. While
for many scientific purposes it is reasonable to use parametric func-
tions like Sérsic or Ferrers functions for fitting structural compo-
nents, GALFIT also allows modeling of curved or irregular struc-
tures. As an illustration of modeling where the spiral arms form
part of the decomposition, a model for NGC 1097 is shown – it
shows a remarkable resemblance to the observed image. We cau-
tion the reader however that since the residuals contain contribu-
tions from partially modeled spiral arms, the model parameters
output by GALFIT are not necessarily ideal for the study of faint
structures in galaxies.

and also well known by a large portion of the astronom-
ical community. Other studies in which software was
developed for similar purposes include Simard (1998);
Pignatelli et al. (2006); Méndez-Abreu et al. (2008).

To simplify the use of GALFIT for a large num-
ber of cases, a set of new IDL-based tools have been
created ("GALFIDL"). They include automatic cre-
ation of the input files for decompositions, contain-
ing reasonable first guesses for the initial parameters
based on P3 products, as well as routines for run-
ning and visualizing the decompositions. GALFIDL
will be available to the community concurrently with
the publication of the data and the GALFIT analyses;
an overview of these procedures is already available at
http://cc.oulu.fi/~hsalo/galfidl.html.

As a standard part of the pipeline analysis, decomposi-
tions include bulges and disks, and, if appropriate, bars,
nuclear components, and in some cases multiple exponen-
tial disks. Taking into account that decompositions, par-
ticularly at high redshift, are often made in a more simple
manner, we also compute the 2-component bulge/disk
decompositions, and 1-component Sérsic function fits. A
decomposition for NGC 1097 is shown in Figs. 8 and
9: the 5-component model includes an exponential disk,
a Sérsic function for the bulge, and a Ferrers function
for the bar. The galaxy has an extremely prominent nu-
clear ring, which is fit using a Gaussian function, and a
nuclear point source using the corresponding PSF. With-
out deep, almost dust-free observations, like those in S^4G
, the measurement of bulge structural parameters, like
shape, size and profile, might in some cases be compro-
mised if the quantification of underlying structures, such
as the disks, bars and rings is inaccurate. GALFIT3.0 al-

lows for even more sophisticated decompositions, which will be made for selected sub-samples of S^{4}G galaxies. For example, it is possible to add more components, or one may want to fit the spiral arms, of which an example is shown in Fig. 10.

6. SCIENCE INVESTIGATIONS

In this section we highlight some preliminary results from a number of science investigations that are and will be carried out by the S^{4}G team. We also discuss possible studies that will be enabled by the S^{4}G dataset.

6.1. *The Faint Outskirts of Galaxies*

A major area of study for S^{4}G is a quantitative analysis of stellar structures in the faint outer regions of galaxies where the stellar surface density we trace is extremely low and comparable or lower than the atomic gas reservoir. Already, deep optical studies have shown that, in a majority of spiral galaxies, the outer disks exhibit a secondary, exponential component. Stellar disks appear to extend beyond 1.5× D$_{25}$ (e.g., Pohlen & Trujillo (2006); Erwin et al. (2008)) with truncated or anti-truncated profiles. *GALEX* (Martin et al. 2005) has found extended UV (XUV) disks even farther out, where it was assumed only H I gas existed (e.g., Gil de Paz et al. (2005); Thilker et al. (2005, 2007); Muñoz-Mateos et al. (2007); Zaritsky & Christlein (2007). Not only is S^{4}G significantly deeper than the previous optical data, but it also traces the stellar profiles into the H I disk of the galaxy – in over 800 S^{4}G galaxies, we image an area >3D$_{25}$.

Another observation that has been much debated is the break between the inner and outer exponentials profiles (e.g., Bakos et al. 2008; Azzollini et al. 2008). With S^{4}G we are measuring the break radius and comparing it to the disk size and mass. The S^{4}G catalog of these breaks will provide strong quantitative constraints for galaxy evolutionary models. In particular, this catalog will be key to quantify the possible role of radial stellar migration in shaping the outskirts of disks (Roškar et al. 2008; Sánchez-Blázquez et al. 2009).

In elliptical galaxies, deep optical observations have revealed the presence of faint tidal tail and shell like structures (e.g., Bennert et al. (2008); Canalizo et al. (2007). S^{4}G contains 188 ellipticals and lenticulars – with this set and the S^{4}G depth we are quantifying the frequency and mass of shells and other debris features in the outskirts of ellipticals and lenticulars.

6.2. *Bulges: Classical, Disk-like, Boxy/Peanut*

Bulges are an inhomogeneous class of objects and different types have been proposed in the literature (Kormendy & Kennicutt 2004; Athanassoula 2005). Kormendy & Kennicutt (2004) distinguishes bulges from pseudo-bulges, while Athanassoula (2005) distinguishes three categories: classical bulges, boxy/peanut bulges, which are a part of a bar, and disk-like bulges, formed out of disk material. Several studies have analyzed their observational properties and compared them with N-body models (e.g. Kuijken & Merrifield 1995; Carollo et al. 1997; Bureau & Freeman 1999; Erwin et al. 2003; Bureau & Athanassoula 2005; Fisher 2006; Drory & Fisher 2007; Fisher & Drory 2008;

Gadotti 2009). Even in lenticular galaxies there seems to be evidence for disk-like bulges, based on structural decompositions (e.g., Laurikainen et al. 2005, 2007; Gadotti 2008; Graham & Worley 2008) and kinematics (e.g., Peletier et al. 2007; Falcón-Barroso et al. 2006). But until now few studies have analyzed the structural properties of bulges in a large number of galaxies; none have done it in a sample as large and deep as S^{4}G . Moreover, S^{4}G encompasses a range of large scale structures, allowing us to examine the environmental influences on the formation of bulges. This may have important implications since massive bulges are expected to form from mergers.

From a preliminary analysis of the S^{4}G data, Buta et al. (2010) are finding that many late type ellipticals in the RC3 have disks, and thus should instead be classified as S0s, consistent with other deep near-infrared studies (Laurikainen et al. 2010). With the S^{4}G data we will examine how common the disk structure is in all types of ellipticals.

Finally, the extremely deep data from S^{4}G allows us to best determine the structural properties of the bulge component – in shallower data, estimates of shape, size and profile are uncertain when measurements of underlying components such as disks, bars and rings are imprecise. As described in §5.4, the S^{4}G project is carrying out detailed decomposition of all the galaxies, and expects to compile the most detailed data base of bulges of all kinds. The combined advantages of the S^{4}G data (deep and insensitive to dust attenuation) and the uniform reduction pipeline (careful and detailed structural analysis) will allow for a suitable examination of galaxies with composite bulges, i.e., galaxies hosting more than one bulge category (e.g., Erwin et al. 2003; Barentine & Kormendy 2009; Nowak et al. 2010). The spatial resolution of our survey is adequate for resolving typical bulges (our resolution is ∼100 pc at the median distance of the survey volume) but is inadequate for precise measurements of the bulge structure from the inability to resolve compact nuclear structures which are often present at the centers of galaxies. These unresolved point sources affect the values of Sersic parameters, which on average are overestimated in ground-based optical images compared to HST studies (e.g., Carollo et al. 1997; Balcells et al. 2003). We also expect that the reduced dust extinction may reveal triaxial structures in bulges, and thus allow us to probe beyond the standard symmetric Sérsic fits.

6.3. *Bars*

Stellar bars are dynamically important structures in galaxies. A bar-induced gas flow leads to a number of evolutionary effects from the triggering of circumnuclear starbursts to the build-up of bulges (Scoville & Hersh 1979; Simkin et al. 1980; Zaritsky & Lo 1986; Athanassoula 1992; Friedli & Benz 1993; Martin & Roy 1994; Friedli & Benz 1995; Sakamoto et al. 1999; Sheth et al. 2000, 2002, 2005). The cosmological redshift evolution of the bar fraction is also an important signpost of the growth and dynamic maturity of galaxies (e.g., Abraham et al. 1999; Sheth et al. 2003; Jogee et al. 2004; Elmegreen et al. 2004; Sheth et al. 2008). Whereas the previous smaller and shallower studies gave mixed results for the change in the bar fraction with redshift, Sheth et al. (2008)

show that not only does the overall bar fraction in
disk galaxies decline significantly over the last seven
billion years, but also that the decline depends on
the galaxy type. They show that the formation and
evolution of bars is strongly correlated with the host
galaxy mass, bulge-dominance and presumably their
dark matter halo. The S⁴G data is critical to establish
the precise local frequency of bars and its variation with
galaxy type. It also provides a measurement of the
light fraction in the bar component (e.g., Durbala et al.
2008; Gadotti 2008; Weinzirl et al. 2009) and accurate
measures of properties such as the bar length, shape
and ellipticity (e.g., Menéndez-Delmestre et al. 2007;
Erwin 2005; Gadotti 2010). Several techniques may
be used to derive bar strengths, based on calculating
bar torques (Laurikainen & Salo 2002; Buta et al.
2003), and estimating the bar-spiral arm contrast
(Elmegreen & Elmegreen 1985). Analysis of the rel-
ative Fourier intensity profiles of bars is compared
with models of the evolution of barred galaxies (e.g.,
Athanassoula & Misiriotis 2002; Debattista et al. 2004)
to constrain the history of their evolution and interaction
with their dark matter halo (Athanassoula 2003).

Another study of interest is the presence of sec-
ondary or nuclear bars which may be responsible for
feeding the central black holes and/or stellar clusters
(Shlosman et al. 1990). The S⁴G observations, unaf-
fected by the high and patchy extinction often present
in galactic centers, allow us to detect all nuclear bars
with sizes of r > 500 pc (our resolution, 2″ ∼ 200 pc at
the median distance of S⁴G) in galaxies of all types.

6.4. Galactic Rings

Outer rings are large, optically low surface brightness
features that dominate the outer disks of some early-
type barred and weakly-barred galaxies (see review by
Buta & Combes (1996). The properties of the rings con-
strain their formation epoch, the dynamical time-scale
at their respective radii, and the evolution of the bar
pattern speed (e.g., Athanassoula (2003). Finding outer
rings around unbarred galaxies is also of great interest,
because it would suggest that some unbarred galaxies
may in fact be highly evolved former barred galaxies.
Whereas ground-based near-IR imaging is rarely deep
enough to detect outer rings reliably to study their stel-
lar populations, colors, and other characteristics, the S⁴G
data will not only allow us to detect many new outer
rings, but also to make a complete census of these fea-
tures in normal galaxies and to measure their stellar
mass, shape, width and ellipticity. Likewise, S⁴G pro-
vides an unprecedented view of circumnuclear and inner
rings, which are typically found in barred spirals. These
rings should have a broad, underlying older stellar pop-
ulation background as they evolve, and it is this type of
feature we will see in the S⁴G data.

6.5. Spiral Arms

A systematic study of spiral arm amplitudes as a func-
tion of radius at 3.6 and 4.5μm, free of confusing ef-
fects from dust extinction, promises to initiate a new
set of spiral arm studies. Although the discrepancies
in the classical density wave model were solved with
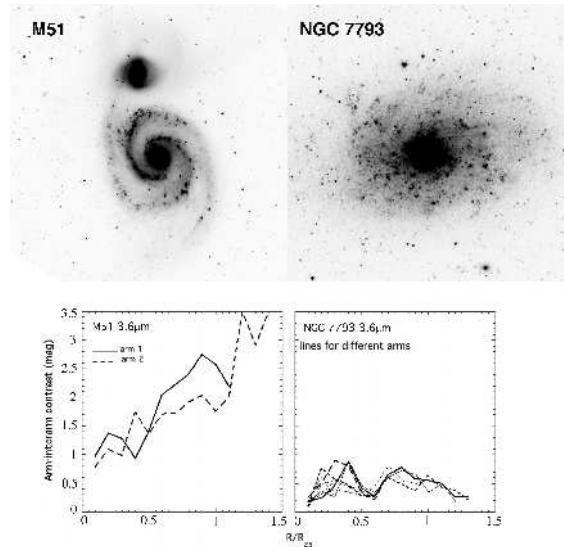the swing amplification theory (Toomre 1981), there

Fig. 11.— Preliminary analysis of the arm-interarm ratios com-
puted for a flocculent spiral, NGC 7793, and a grand design spiral,
M51, from the S⁴G 3.6μm data. Note the increasing contrast in the
grand design galaxy compared to the flocculent galaxy. Detailed
analysis of the stellar density variations will shed important light
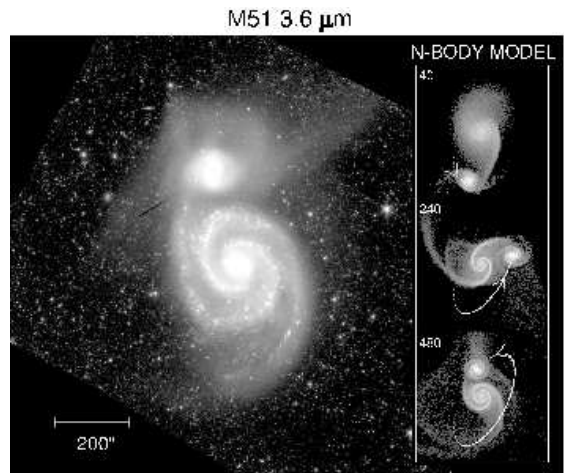on spiral density wave theories.

Fig. 12.— Comparison of the M51 3.6 micron image with the
N-body simulation model of Salo & Laurikainen (2000a,b). The
right hand column shows the simulation at 40, 240 and 480 Myr
from the top to the bottom panels respectively. In the model the
near-IR and rotation curve data existing at the time were used for
setting up the initial disk and halo models. The simulation creates
an outer southern tail when the companion (with mass ratio 0.55)
crosses the primary disk towards the observer about 480 Myr ago.
To obtain the observed apparent counter-rotating HI kinematics,
the tail has a tilt of nearly 40 degrees with respect to the inner
disk. The most recent disk plane crossing about 100 Myr ago is
responsible for the ejecta north of the companion, drawn from the
primary disk, and visible in the S⁴G image. During the prolonged
interaction the tidal wave induced by the direct perturbation is
able to propagate to the central regions, consistent with the inner
spiral structure described by Zaritsky et al. (1993).

has been very little testing of this theory with obser-
vations. Modal studies by Bertin et al. (1989a,b) pre-
dict that there should be amplitude variations along
the arms from resonances between inward and outward
moving spiral waves and the precise amplitude varia-
tions have been modeled (Elmegreen & Elmegreen 1984;
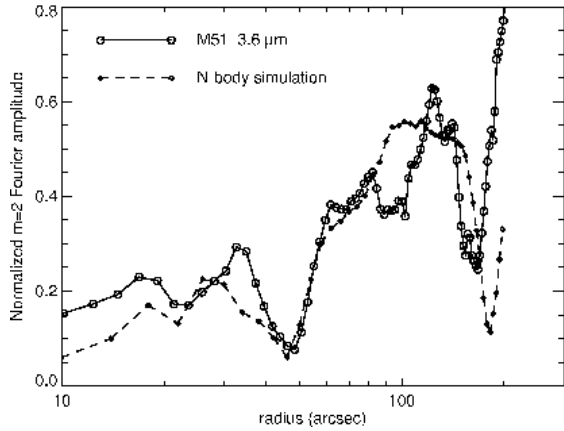Elmegreen et al. 1989; Elmegreen & Thomasson 1993;

FIG. 13.— Comparison of the m=2 Fourier amplitude profile of M51 extracted from S^4G 3.6μm image with the N-body simulations of Salo & Laurikainen (2000a,b). The simulation corresponds to the final snapshot of Fig. 12. The outermost observed minimum at $r \approx 180$ arcsec is related to the change of the curvature of arms: in simulations a similar feature marks the region where the self-gravity sustained spiral wave separates from purely tidal outer structure. In the model the minima at $r \approx 40$ and 20 arcsec are amplitude modulations, which arise due to interference between separate inward-propagating tidal wave packets. See also Figure 11 for M51 at $R_{25} \approx 300''$

Regan & Elmegreen 1997). Most recently, a new theory has been proposed for the formation of rings and spiral arms which argues in favor of chaotic orbits, confined by invariant manifolds emanating from the L1 & L2 Lagrangian points of a bar (Romero-Gómez et al. 2007). Several comparisons between the results of this theory and observations have been carried out successfully (Athanassoula et al. 2009b,a) and several more will be possible with the S⁴G database. S⁴G will cover the full range of galaxies with varying spiral arm strengths and galactic structures. In Figure 11, we show a preliminary result of the type of analysis that is possible with the S⁴G data. In this figure we show the arm-interarm contrast measured from the 3.6μm S⁴G images for NGC 7793, a flocculent galaxy, in contrast with M51, a grand design spiral galaxy (see a model for amplitude variation of M51 in Salo & Laurikainen 2000a). The contrasts are measured beyond R$_{25}$, further than in previous optical studies. The spiral structure traced in the 3.6 μm band is different in detail from the optical images, but still shows weak arms in NGC 7793 and increasingly stronger arms in M51. We will carry out a detailed analysis of spiral arm amplitudes and variations and compare the observational data to the models.

For the NGC 5194 (M51) system, there may well be a connection between the spiral structure and the presence of the companion (NGC 5195). Indeed, detailed HI observations by Rots et al. (1990) show the presence of a long tail, which emanates from the west side of the galaxy, running south of the spiral arm visible in the S⁴G image, and turning up towards the north further eastwards. The HI kinematics are very difficult to model with an interaction involving a single passage, but Salo & Laurikainen (2000a,b) propose a model with a second passage (Figure 12), which gives a better fit to some of the aspects of the observations. The inner spiral structure in the main spiral is then amplified by the action of the companion, and wave interference causes amplitude modulations, which are well reproduced in the

S⁴G observations (Figure 13). This shows the interest of the S⁴G data for detailed modeling of the dynamics of individual galaxies.

6.6. Early Type Galaxies & Dwarfs

S⁴G contains 188 galaxies of T-type < 0 and therefore constitutes one of the largest and most homogeneous mid-infrared data sets for early type galaxies. The shapes of ellipticals and lenticulars may reflect different evolutionary paths, with wet mergers leading to disky shapes and dry mergers leading to boxy profiles (Naab et al. 2006; Pasquali et al. 2007; Kang et al. 2007). In addition, Kormendy et al. (2009) shows that deep imaging can reveal departures from the Sérsic profiles in elliptical galaxies, which are diagnostics of their formation. They found a dichotomy in which ellipticals that have cuspy cores at their inner radii can be separated from those which show an excess of light at the center. The S⁴G data offer us a unique opportunity to revisit the frequency of the different shapes and profiles as a function of stellar mass and environment, free of dust obscuration effects.

Although dwarfs are the most abundant type of galaxy in the Universe, their low surface brightnesses of typically $\mu_B > 22$ mag arcsec^{-2} have restricted detailed observations of these stellar systems. In particular, the characterization of the underlying stellar structure in these faint galaxies still remains largely unexplored. Using an absolute magnitude criterion of $M_B > -17$, we have identified a preliminary sample of 206 dwarf galaxies in S⁴G . The sample includes 87 late-type DDO dwarfs previously unobserved with *Spitzer*, to complement the 48 which have been observed. The S⁴G dwarfs therefore constitute a representative sample of nearby dwarf galaxies in which to study the properties of the underlying stellar component.

Dwarf galaxies in S⁴G allow for a detailed analysis of the underlying stellar disk in both the 3.6 and 4.5μm data. By deriving the radial scale lengths for these galaxies, more insight can be gained into the evolutionary link between dwarfs and their giant counterparts. At the same time, the relatively large sample of dwarfs in S⁴G gives a unique opportunity to look at how these parameters may vary with environment. We can also derive stellar masses for the dwarfs which will be used to assess their stellar mass to dark-matter ratio and will likely provide crucial evidence to the longstanding debate of whether these galaxies are truly dark-matter dominated systems (see e.g., Strigari et al. 2008).

In addition to these areas, there are at least three other main areas of astrophysics that these data will address uniquely: the reported absence of bulges in some disk galaxies, the vertical stellar structure, and the Tully-Fisher relationship. There is also likely to be significant amounts of spin-off science for S⁴G with its large and accurate inventory of mass and galactic structure in the nearby Universe, e.g., relationship between the Tully-Fisher relationship and properties of the fundamental plane (e.g., Zaritsky et al. 2008), dust heating in outer disks, the interaction / merger fraction from a study of the debris around these galaxies, and diagnosis of AGN activity from tracing hot dust very close to the AGN from the [3.6]-[4.5] color.

7. DATA RELEASE AND TEAM POLICY

The S^{4}G team is committed to releasing all of the reduced data upon publication of the entire S^{4}G datasets from each of the pipelines. We expect the science-ready images from pipeline 1, the masks from pipeline 2, the galaxy properties and profiles from pipeline 3 and the input and output files from Pipeline 4 (including the mask, sigma images, images without NaN values and the GALFIT input and output parameter files) to be released on a staggered schedule using NED or IRSA for long term use by the community. Currently the products of each of the pipeline are expected to be released in the supplement issue of the journals upon verification of their quality which will be on-going and occur as part of the various scientific investigations conducted by the team. We expect that some of the data and pipeline may need to be refined or enhanced in the future. As the data are still being acquired (data acquisition is expected to be complete in 2011) and analyzed, our earliest release date for the the science-ready images (P1 products) for the entire S^{4}G data is not expected at least until 2012, and the supplement papers for the products from the other pipelines are expected to follow within a year after the Pipeline 1 supplement paper. In the meanwhile, to allow for maximum use of the data for science by the larger community, the collaboration has agreed on an open-door policy whereby any member of the astronomical community may join the team temporarily as a guest and pursue any type of science. The use of the data, publication policies and authorship on papers are clearly defined in our policy statement available here: `http://www.cv.nrao.edu/~ksheth/s4g/S4G_policy_v6.pdf`. This statement is adopted by the S^{4}G team and all of its guests. Interested members of the astronomical community are invited to read the policy and contact the PI or an S^{4}G member to discuss the possibilities of joining the team.

The noteworthy point of this policy is that our team has agreed to avoid carving out large science categories or areas to encourage the maximum use of the data within the team, and within the larger community, for any science that may be possible with these data. Our philosophy is that if multiple people are interested in a topic but want to work in separate teams then we will encourage both teams to collaborate and address the scientific problems in independent but parallel investigations.

8. SUMMARY

S^{4}G will provide the deepest, largest, and most homogenous data set of nearby galaxies at 3.6 and 4.5μm. The spatial resolution will be unmatched at these wavelengths, $\sim2''$, which is ideal for comparisons to ground based optical and near-IR observations, as well as MeerKAT, eVLA, ALMA and other future large radio array surveys. The sample of 2,331 galaxies includes most morphological types and masses. The images will give an unparalleled view of stellar mass distributions and faint peripheral structures. All of the galaxies, as well as many additional galaxies from the *Spitzer* archives, will be reduced in the same way, giving data products that span the full range from science-ready images to measurements of global galaxy properties and individual components. S^{4}G is designed to be a useful reference for many years to come. It will contain the best available mid-infrared data for individual galaxies and be among the most complete surveys for statistical studies. It will be useful to study the origin and evolution of galaxies and their dynamical components, and to supplement observations of nearby galaxies at other wavelengths.

Facilities: Spitzer Space Telescope

REFERENCES

Abraham, R. G., Merrifield, M. R., Ellis, R. S., Tanvir, N. R., & Brinchmann, J. 1999, MNRAS, 308, 569
Athanassoula, E. 1992, MNRAS, 259, 345
—. 2003, MNRAS, 341, 1179
—. 2005, MNRAS, 358, 1477
Athanassoula, E., & Misiriotis, A. 2002, MNRAS, 330, 35

Athanassoula, E., Romero-Gómez, M., Bosma, A., & Masdemont, J. J. 2009a, MNRAS, 400, 1706
Athanassoula, E., Romero-Gómez, M., & Masdemont, J. J. 2009b, MNRAS, 394, 67
Azzollini, R., Trujillo, I., & Beckman, J. E. 2008, ApJ, 684, 1026
Bakos, J., Trujillo, I., & Pohlen, M. 2008, ApJ, 683, L103

Balcells, M., Graham, A. W., Domínguez-Palmero, L., & Peletier, R. F. 2003, ApJ, 582, L79

Barentine, J. C., & Kormendy, J. 2009, ArXiv e-prints

Barnes, D. G., et al. 2001, MNRAS, 322, 486

Bell, E. F., McIntosh, D. H., Katz, N., & Weinberg, M. D. 2003, ApJS, 149, 289

Bennert, N., Canalizo, G., Jungwiert, B., Stockton, A., Schweizer, F., Peng, C. Y., & Lacy, M. 2008, ApJ, 677, 846

Bertin, E., & Arnouts, S. 1996, A&AS, 117, 393

Bertin, G., Lin, C. C., Lowe, S. A., & Thurstans, R. P. 1989a, ApJ, 338, 78

—. 1989b, ApJ, 338, 104

Bureau, M., & Athanassoula, E. 2005, ApJ, 626, 159

Bureau, M., & Freeman, K. C. 1999, AJ, 118, 126

Buta, R., Block, D. L., & Knapen, J. H. 2003, AJ, 126, 1148

Buta, R., & Combes, F. 1996, Fundamentals of Cosmic Physics, 17, 95

Buta, R. J., et al. 2010, ApJ, submitted

Canalizo, G., Bennert, N., Jungwiert, B., Stockton, A., Schweizer, F., Lacy, M., & Peng, C. 2007, ApJ, 669, 801

Carollo, C. M., Stiavelli, M., de Zeeuw, P. T., & Mack, J. 1997, AJ, 114, 2366

Dalcanton, J. J., et al. 2009, ApJS, 183, 67

de Vaucouleurs, G., Corwin, Jr., H. G., & Bollinger, G. 1977, ApJS, 33, 229

de Vaucouleurs, G., de Vaucouleurs, A., Corwin, Jr., H. G., Buta, R. J., Paturel, G., & Fouque, P. 1991, Third Reference Catalogue of Bright Galaxies, ed. de Vaucouleurs, G., de Vaucouleurs, A., Corwin, H. G., Jr., Buta, R. J., Paturel, G., & Fouque, P.

Debattista, V. P., Carollo, C. M., Mayer, L., & Moore, B. 2004, ApJ, 604, L93

Draine, B. T., & Lee, H. M. 1984, ApJ, 285, 89

Drory, N., & Fisher, D. B. 2007, ApJ, 664, 640

Durbala, A., Sulentic, J. W., Buta, R., & Verdes-Montenegro, L. 2008, ArXiv e-prints, 0807.2216

Elmegreen, B. G., & Elmegreen, D. M. 1985, ApJ, 288, 438

Elmegreen, B. G., Elmegreen, D. M., & Hirst, A. C. 2004, ApJ, 612, 191

Elmegreen, B. G., Seiden, P. E., & Elmegreen, D. M. 1989, ApJ, 343, 602

Elmegreen, B. G., & Thomasson, M. 1993, A&A, 272, 37

Elmegreen, D. M., & Elmegreen, B. G. 1984, ApJS, 54, 127

Epchtein, N., et al. 1994, Ap&SS, 217, 3

Erwin, P. 2005, MNRAS, 364, 283

Erwin, P., Beltrán, J. C. V., Graham, A. W., & Beckman, J. E. 2003, ApJ, 597, 929

Erwin, P., Pohlen, M., & Beckman, J. E. 2008, AJ, 135, 20

Eskridge, P. B., et al. 2002, ApJS, 143, 73

Falcón-Barroso, J., et al. 2006, New Astronomy Review, 49, 515

Fazio, G. G., et al. 2004, ApJS, 154, 10

Fisher, D. B. 2006, ApJ, 642, L17

Fisher, D. B., & Drory, N. 2008, AJ, 136, 773

Friedli, D., & Benz, W. 1993, A&A, 268, 65

—. 1995, A&A, 301, 649

Gadotti, D. A. 2008, MNRAS, 384, 420

—. 2009, MNRAS, 393, 1531

—. 2010, ArXiv e-prints

Gil de Paz, A., et al. 2005, ApJ, 627, L29

—. 2007, ApJS, 173, 185

Giovanelli, R., et al. 2005, AJ, 130, 2598

Graham, A. W., & Worley, C. C. 2008, MNRAS, 388, 1708

Heraudeau, P., & Simien, F. 1997, A&A, 326, 897

Jarrett, T. 2004, Publications of the Astronomical Society of Australia, 21, 396

Jogee, S., et al. 2004, ApJ, 615, L105

Jun, H. D., & Im, M. 2008, ApJ, 678, L97

Kang, X., van den Bosch, F. C., & Pasquali, A. 2007, MNRAS, 381, 389

Kennicutt, Jr., R. C., et al. 2003, PASP, 115, 928

Kent, S. M. 1985, ApJS, 59, 115

Kormendy, J., Fisher, D. B., Cornell, M. E., & Bender, R. 2009, ApJS, 182, 216

Kormendy, J., & Kennicutt, Jr., R. C. 2004, ARA&A, 42, 603

Kuijken, K., & Merrifield, M. R. 1995, ApJ, 443, L13

Laurikainen, E., & Salo, H. 2002, MNRAS, 337, 1118

Laurikainen, E., Salo, H., & Buta, R. 2005, MNRAS, 362, 1319

Laurikainen, E., Salo, H., Buta, R., & Knapen, J. H. 2007, MNRAS, 381, 401

—. 2009, ApJ, 692, L34

Laurikainen, E., Salo, H., Buta, R., Knapen, J. H., & Comerón, S. 2010, MNRAS, 405, 1089

Lee, J. C., et al. 2008, in Astronomical Society of the Pacific Conference Series, Vol. 396, Astronomical Society of the Pacific Conference Series, ed. J. G. Funes & E. M. Corsini, 151—+

Martin, D. C., et al. 2005, ApJ, 619, L1

Martin, P., & Roy, J.-R. 1994, ApJ, 424, 599

Méndez-Abreu, J., Aguerri, J. A. L., Corsini, E. M., & Simonneau, E. 2008, A&A, 478, 353

Menéndez-Delmestre, K., Sheth, K., Schinnerer, E., Jarrett, T. H., & Scoville, N. Z. 2007, ApJ, 657, 790

Muñoz-Mateos, J. C., Gil de Paz, A., Boissier, S., Zamorano, J., Jarrett, T., Gallego, J., & Madore, B. F. 2007, ApJ, 658, 1006

Muñoz-Mateos, J. C., et al. 2009, ApJ, 703, 1569

Naab, T., Khochfar, S., & Burkert, A. 2006, ApJ, 636, L81

Nowak, N., Thomas, J., Erwin, P., Saglia, R. P., Bender, R., & Davies, R. I. 2010, MNRAS, 106

Oke, J. B. 1974, ApJS, 27, 21

Pahre, M. A., Ashby, M. L. N., Fazio, G. G., & Willner, S. P. 2004, ApJS, 154, 235

Pasquali, A., van den Bosch, F. C., & Rix, H. 2007, ApJ, 664, 738

Paturel, G., Petit, C., Rousseau, J., & Vauglin, I. 2003, VizieR Online Data Catalog, 340, 50001

Peletier, R. F., et al. 2007, New Astronomy Review, 51, 29

Peng, C. Y., Ho, L. C., Impey, C. D., & Rix, H. 2002, AJ, 124, 266

—. 2010, AJ, 139, 2097

Pignatelli, E., Fasano, G., & Cassata, P. 2006, A&A, 446, 373

Pohlen, M., & Trujillo, I. 2006, A&A, 454, 759

Regan, M. W., & Elmegreen, D. M. 1997, AJ, 114, 965

Regan, M. W., & Teuben, P. J. 2004, ApJ, 600, 595

Regan, M. W., et al. 2006, ApJ, 652, 1112

Rhoads, J. E. 1998, AJ, 115, 472

Romero-Gómez, M., Athanassoula, E., Masdemont, J. J., & García-Gómez, C. 2007, A&A, 472, 63

Rots, A. H., Bosma, A., van der Hulst, J. M., Athanassoula, E., & Crane, P. C. 1990, AJ, 100, 387

Roškar, R., Debattista, V. P., Stinson, G. S., Quinn, T. R., Kaufmann, T., & Wadsley, J. 2008, ApJ, 675, L65

Sakamoto, K., Okumura, S. K., Ishizuki, S., & Scoville, N. Z. 1999, ApJ, 525, 691

Salo, H., & Laurikainen, E. 2000a, MNRAS, 319, 377

—. 2000b, MNRAS, 319, 393

Sánchez-Blázquez, P., Courty, S., Gibson, B. K., & Brook, C. B. 2009, MNRAS, 398, 591

Scoville, N. Z., & Hersh, K. 1979, ApJ, 229, 578

Sheth, K., Regan, M. W., Scoville, N. Z., & Strubbe, L. E. 2003, ApJ, 592, L13

Sheth, K., Regan, M. W., Vogel, S. N., & Teuben, P. J. 2000, ApJ, 532, 221

Sheth, K., Vogel, S. N., Regan, M. W., Teuben, P. J., Harris, A. I., & Thornley, M. D. 2002, AJ, 124, 2581

Sheth, K., Vogel, S. N., Regan, M. W., Thornley, M. D., & Teuben, P. J. 2005, ApJ, 632, 217

Sheth, K., et al. 2008, ApJ, 675, 1141

Shlosman, I., Begelman, M. C., & Frank, J. 1990, Nature, 345, 679

Simard, L. 1998, in Astronomical Society of the Pacific Conference Series, Vol. 145, Astronomical Data Analysis Software and Systems VII, ed. R. Albrecht, R. N. Hook, & H. A. Bushouse, 108—+

Simkin, S. M., Su, H. J., & Schwarz, M. P. 1980, ApJ, 237, 404

Skrutskie, M. F., et al. 2006, AJ, 131, 1163

Strigari, L. E., Bullock, J. S., Kaplinghat, M., Simon, J. D., Geha, M., Willman, B., & Walker, M. G. 2008, Nature, 454, 1096

Thilker, D. A., et al. 2005, ApJ, 619, L79

—. 2007, ApJS, 173, 538

Tokunaga, A. T., Sellgren, K., Smith, R. G., Nagata, T., Sakata, A., & Nakada, Y. 1991, ApJ, 380, 452

Toomre, A. 1981, in Structure and Evolution of Normal Galaxies, ed. S. M. Fall & D. Lynden-Bell, 111–136

Weinzirl, T., Jogee, S., Khochfar, S., Burkert, A., & Kormendy, J. 2009, ApJ, 696, 411

Werner, M. W., et al. 2004, ApJS, 154, 1

TABLE 1
The S⁴G Sample.

Galaxy	RA (J2000)	DEC (J2000)	T	M_B	Log(D_{25})	m_{Bcorr}
UGC12893	0.00784	17.21952	8.4	-15.97	1.06	15.14
PGC000143	0.03292	-15.46140	9.9	-15.83	2.04	10.00
ESO012-014	0.04511	-80.34825	9.0	-18.17	1.18	13.72
NGC7814	0.05418	16.14554	2.0	-20.04	1.64	10.96
UGC00017	0.06198	15.21822	9.0	-16.02	1.39	14.60
NGC7817	0.06635	20.75182	4.1	-21.11	1.52	11.56
ESO409-015	0.09223	-28.09915	6.2	-15.16	1.02	14.43
ESO293-034	0.10559	-41.49592	6.0	-18.68	1.40	12.67
NGC0007	0.13916	-29.91678	4.9	-18.22	1.39	13.18
NGC0014	0.14618	15.81659	9.8	-18.25	1.18	12.35
IC1532	0.16464	-64.37161	4.0	-17.89	1.26	13.86
...	...	...	...	...	...	...
...	...	...	...	...	...	...
NGC7798	23.99042	20.74986	4.1	-20.20	1.20	12.56
NGC7800	23.99354	14.80723	9.7	-19.45	1.24	12.61

NOTE. — The full table is available in the electronic version of the journal.

TABLE 2
Sample RC3-like parameters

Galaxy	μ	3.6μm sma	ellip.	PA	4.5μm sma	ellip.	PA
NGC 0337	25.5	90.6±1.5	0.287±0.018	118.4±2.0	84.1±1.3	0.278±0.037	118.5±4.5
	26.5	110.4±4.7	0.270±0.027	119.8±3.2	106.9±1.3	0.287±0.055	123.8±7.1
NGC 4450	25.5	209.0±6	0.293±0.016	1.4±1.8	199.9±...	0.293±0.020	3.2±2.3
	26.5	253.0±6	0.336±0.048	19.8±5.1	266.7±...	0.418±0.026	18.1±2.3
NGC 4579	25.5	256.0±2.6	0.295±0.011	95.2±1.2	229.0±2.6	0.268±0.018	95.5±2.2
	26.5	278.6±17	0.251±0.018	78.6±2.4	263.4±12	0.282±0.027	98.3±3.4

NOTE. — RC3-like parameters for three sample galaxies. For each galaxy and band we quote the semi-major axis (in arcseconds), the ellipticity and the position angle (in degrees) at two levels of surface brightness: 25.5 and 26.5 (AB) mag arcsec^{-2}. The error in the semi-major axis is measured by noting the change in the corresponding radius when the surface brightness profiles are shifted up and down by the local measurement error plus 10% additional error, which is the maximum expected from any scattered light on the detector. For NGC 4450, the error cannot be measured due to contamination from a background star and is therefore set to the maximum error, 6″, as discussed in the text. The errors in the ellipticity and position angle are from the ellipse fitting and reflect the rms in the formal fit of the corresponding isophote. These errors are significantly larger than any error introduced by the shifting the profiles to measure the error in semi-major axis.

TABLE 3
Magnitudes and Concentration Indices for S⁴G Galaxies

Galaxy	3.6μm mag (AB)	C_{31}	C_{42}	4.5μm mag (AB)	C_{31}	C_{42}
NGC 0337	11.432±0.001	2.67	2.74	11.888±0.002	2.82	2.90
NGC 4450	9.630±0.001	4.58	4.17	10.112±0.001	4.56	4.16
NGC4579	9.083±0.001	5.29	4.54	9.564±0.001	5.60	4.71

Worthey, G. 1994, ApJS, 95, 107
Zaritsky, D., & Christlein, D. 2007, AJ, 134, 135
Zaritsky, D., & Lo, K. Y. 1986, ApJ, 303, 66

Zaritsky, D., Rix, H., & Rieke, M. 1993, Nature, 364, 313
Zaritsky, D., Zabludoff, A. I., & Gonzalez, A. H. 2008, ApJ, 682, 68